

8 Schmidt Propeller

In this chapter, the transient aerodynamic loading of a passing *mushroom wake* on a static hindfoil is examined experimentally using control-volume and pressure-integration analyzes. The results can then be used as a reference for the full tandem interactions examined in the subsequent chapter where the hindfoil oscillates in the vortical wake.

8.1 Parameter Space

The Schmidt-propeller configuration used in this study consisted of an oscillating forefoil and a static hindfoil positioned at $x/c = 2$ in its wake (distance measured between quarter-chord positions). The forefoil was oscillated with a so-called *pure-plunge* motion based on a simple harmonic motion:

$$h(t) = h_o \cos(2\pi ft), \quad (8.1)$$

where h is the time-dependent plunge position, h_o the plunge amplitude and f the frequency of the period. A geometric angle of attack of 8° was used since at this reduced frequency of $k = 0.25$ strong LEV-TEV vortex pairs were found to be repeatedly shed into the wake. The plunge amplitude of $h_o = 0.5c$ was also held constant. An analogous pure-pitch motion with a mean angle of attack of 8° was tested and found to produce a very similar vortex wake, yet slightly more compact than that of the pure-plunge motion. For a detailed comparison of these two motions please refer to section 5.2.2. The hindfoil had three static vertical offsets (h/c) relative to the forefoil centerline. The first position corresponded to the center position of the forefoil's stroke ($h/c = 0$), the second position was at the quarter-stroke position ($h/c = -0.25$) and the third position at bottom-dead-center ($h/c = -0.5$). The angle of attack of the hindfoil was varied between $\alpha_H = 0^\circ$ and $\alpha_H = 8^\circ$.

8.2 Results

8.2.1 Trajectories and Convective Velocities

The wakes of two single-airfoil reference cases and five tandem test cases have been captured, where the kinematics of the forefoil are based on the studies in section 5.2.2, referred to as pure-plunge 8° (single) and pure-pitch 8° (single). The angle of attack (α_H) and relative positioning (h/c) of the hindfoil to the centerline are given in brackets in the corresponding figure legends. Cases with $\alpha_H = 0^\circ$ are referred to as *unloaded* cases since the hindfoil at this incidence produces negligible lift. Conversely cases with $\alpha_H = 8^\circ$ are considered *loaded* since the hindfoil at this incidence generates considerable lift. However, for the latter case the flow is on the verge of stall and is therefore very sensitive to the vortex-blade interaction examined here.

By tracking the trajectories of the wake vortices, see Fig. 1(a) and (b), the nature of the blade-vortex interaction for the various cases can be examined. Here the effect of the hindfoil circulation - proportional primarily to the hindfoil angle of attack α_H - causes the shed vortices to shift upwards in the wake as they travel downstream. Subsequently

the convective velocities of these vortices have been extracted, as shown in Fig. 2(a) and (b). Here the convective velocities show very similar trends, with the exception of the pure-plunge 8° ($h/c = -0.25, 0^\circ$) case where both LEV and TEV exhibit strong viscous interactions with the hindfoil. In this case the LEV passes much closer to the airfoil surface such that the vortex core distance to the surface is $y/c \simeq 0.25$ instead of $y/c \simeq 0.5$ for $h/c = -0.5$. This close proximity in turn decelerates the vortex due to the generation of a strong image or mirror vortex below the hindfoil's surface, a phenomenon described in Doligalski et al (1994). Furthermore, for this unloaded case no separation is induced at the leading edge and therefore the vortex is dissipated more quickly. For the equivalent loaded blade interaction, the separated region at the leading edge shields the LEV from the wall's dissipative effects. Wilder and Telionis (1998) came across this shielding effect of the leading-edge shear layer in their studies when comparing the vortex-blade interactions between both unloaded and loaded cases. In the following section the dissipation due to vortex interaction with the hindfoil has been quantified and tracked over time.

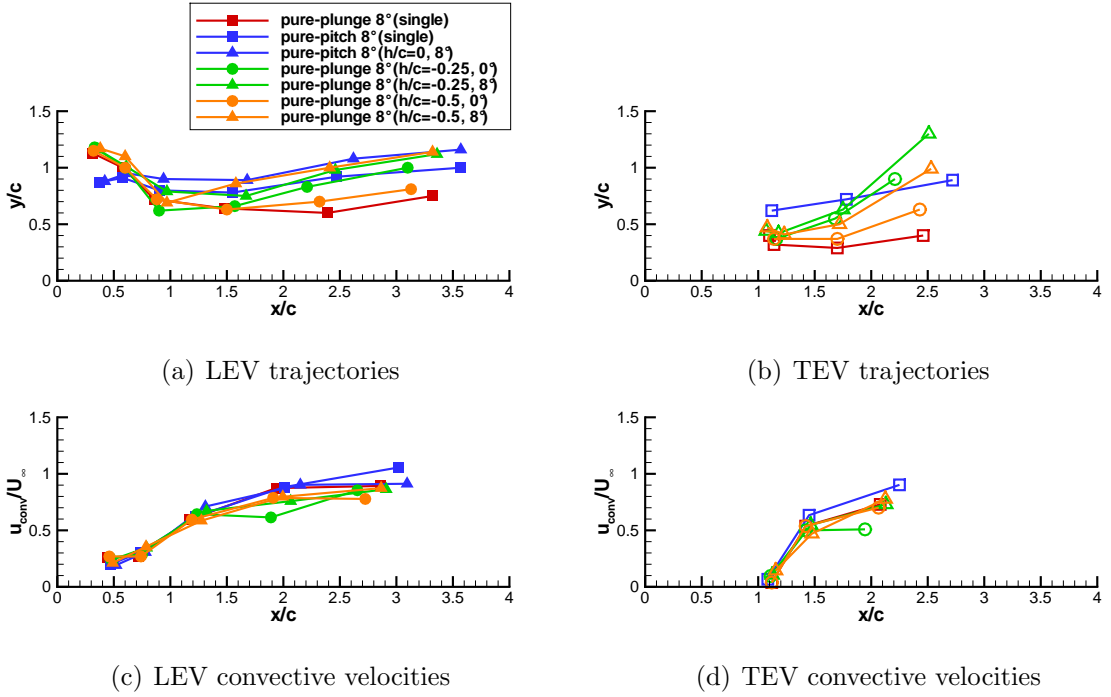


Figure 8.1: Measured trajectories and convective velocities of LEV and TEV cores for the various single-airfoil and tandem-airfoil configurations; note h/c refers to vertical orientation of hindfoil.

8.2.2 Vortex Circulation

In Fig. 8.2 the temporal evolution of both LEV and TEV circulation has been plotted over the cycle. As reported on in chapter 6, the LEV is found to reach its maximum circulation just before pinch-off from the leading-edge shear layer. Of interest here for the tandem configurations is the substantial strengthening of the LEV in comparison to the single-airfoil reference case, particularly for the cases with $\alpha_H = 8^\circ$. This strengthening is due to the circulation of the hindfoil in the forefoil's wake, which has the effect of increasing the size of the developing LEV. In turn the TEV is strengthened by the induction of the LEV as it passes over the trailing edge. Also noteworthy is the drastic

break-up of the LEV for the tandem configurations with $h/c = -0.25$. For these cases the vortex passes very closely over the hindfoil surface and therefore is dissipated more rapidly, as described by Wilder and Telionis (1998).

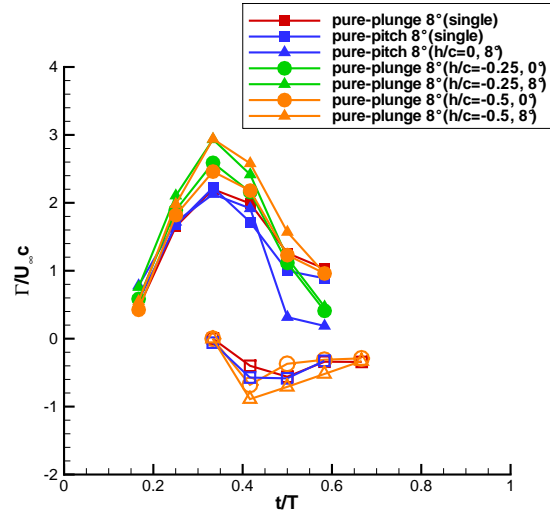


Figure 8.2: Development of LEV and TEV circulation as a function of period for the various single-airfoil and tandem-airfoil configurations; note solid and hollow symbols represent LEVs and TEVs, respectively.

8.2.3 Vortex-Induced Separation

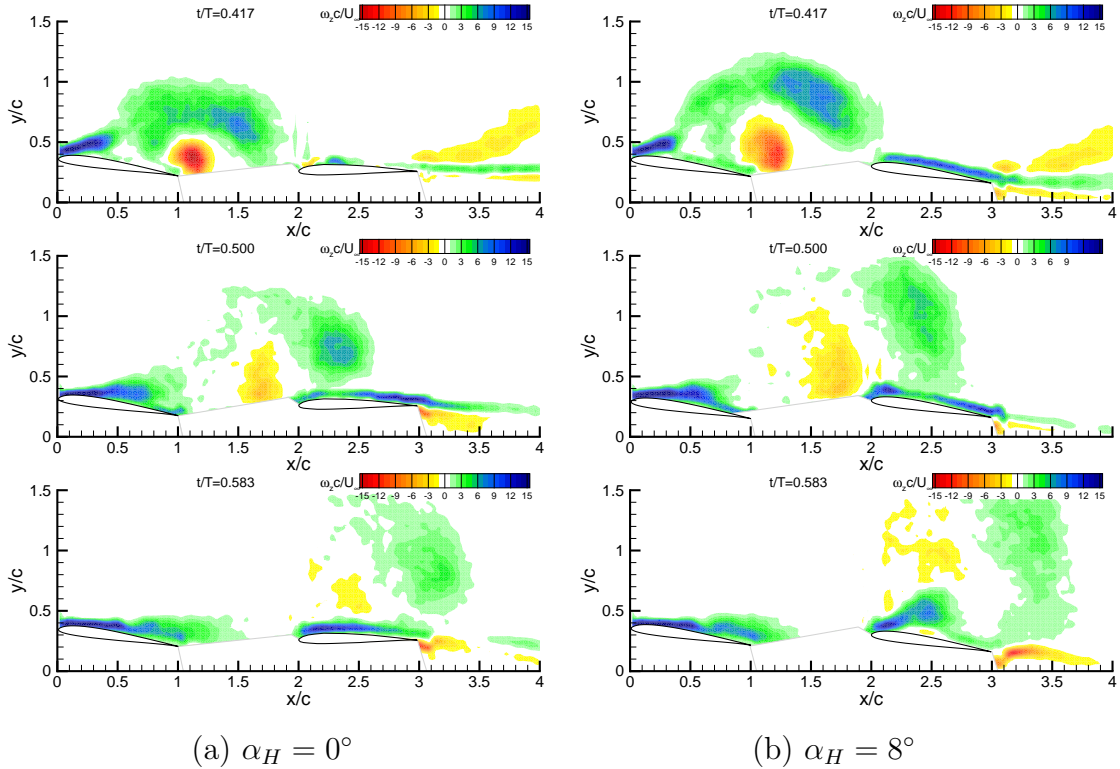


Figure 8.3: Comparison of blade-vortex interaction between unloaded and loaded cases; (a) $h/c = -0.5$ and $\alpha_H = 0^\circ$, and (b) $h/c = -0.5$ and $\alpha_H = 8^\circ$.

For certain cases when the hindfoil is loaded and thus near its stall limit, i.e. $\alpha_H = 8^\circ$, a vortex-induced separation occurs when the TEV passes close over the hindfoil leading edge. The TEV with its counter-clockwise rotation generates an upwash at the leading edge. This in turn induces a boundary-layer separation analogous to dynamic stall leading to the roll-up of a clockwise-oriented LEV. This effect could be best observed for the pure-plunge 8° ($h/c = -0.5, 8^\circ$) case, as shown in Fig. 8.3(b). This stark contrast between unloaded ($\alpha_H = 0^\circ$) versus loaded ($\alpha_H = 8^\circ$) cases has also been observed in the blade-vortex interaction studies of Wilder and Telionis (1998).

In Fig. 8.4 a similar comparison between unloaded and loaded blade-vortex interaction can be made, albeit the vertical spacing of the hindfoil is such that the TEV impacts the leading edge and dissipates rapidly. In Fig. 8.4(a), leftover portions of the TEV pass over both surfaces of the hindfoil into the wake. Before the occurrence of this strong viscous interaction ($t/T = 0.417$ and $t/T = 0.5$), the approaching TEV clearly induces a separation at the hindfoil leading edge for the pure-plunge 8° ($h/c = -0.25, 8^\circ$) case.

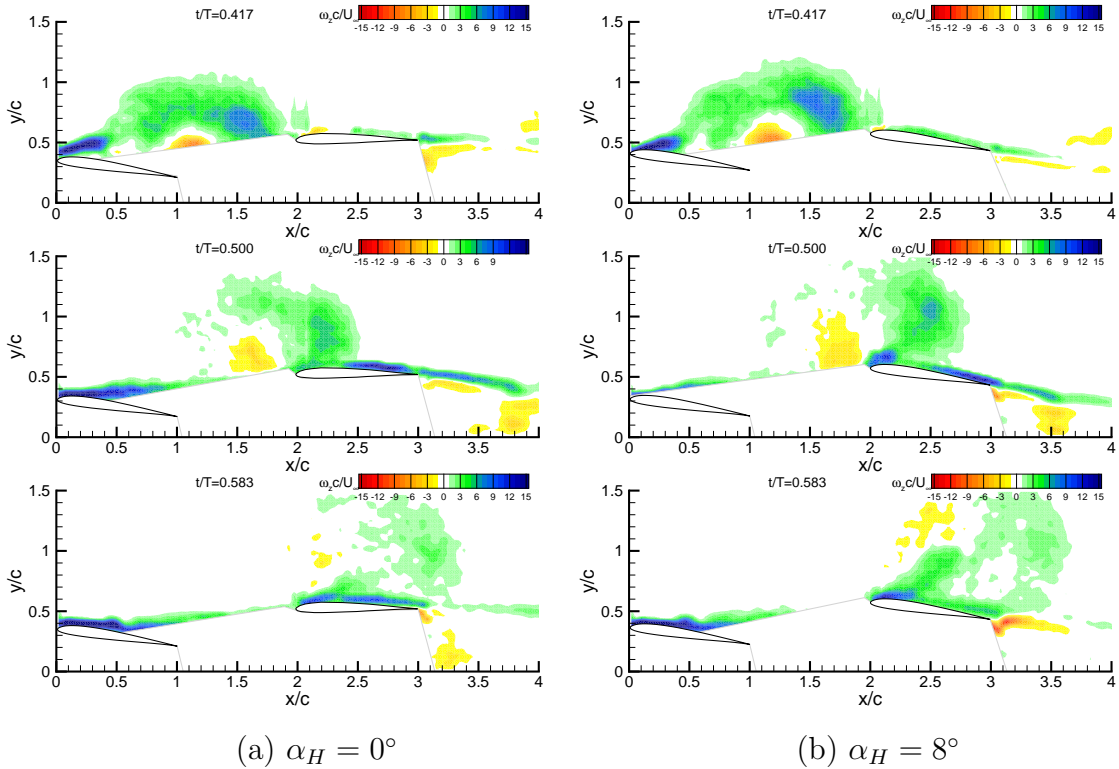


Figure 8.4: Comparison of blade-vortex interaction between unloaded and loaded cases; (a) $h/c = -0.25$ and $\alpha_H = 0^\circ$, and (b) $h/c = -0.25$ and $\alpha_H = 8^\circ$.

8.2.4 Control-Volume Analysis

In Table 8.1, a summary of the combined lift and drag coefficients for the various tandem configurations is presented. Interestingly the tandem configurations show combined values of lift similar to levels of two separate airfoils (pure-plunge plus static), refer to Table 3.1 for individual values. This suggests that any increase in lift due to vortex interaction is canceled out by the subsequent vortex-induced separation. However, when examining drag for the pure-pitch 8° ($h/c = 0, 8^\circ$) case, a substantial increase can be observed. Conversely for the other Schmidt cases drag is reduced, albeit by a very minor amount. This net thrust increase on the hindfoil can be explained by vortical interaction at the leading edge, i.e. leading-edge suction, as first measured by Schmidt (1965).

Table 8.1: Comparison of lift and drag coefficients for the various cases.

case	C_l (PIV)	C_d (PIV)
pure-plunge 8° (single)	0.88	0.09
pure-pitch 8° (single)	0.91	0.18
pure-pitch 8° ($h/c = 0, 8^\circ$)	1.66	0.32
pure-plunge 8° ($h/c = -0.25, 0^\circ$)	0.93	0.13
pure-plunge 8° ($h/c = -0.25, 8^\circ$)	1.60	0.15
pure-plunge 8° ($h/c = -0.5, 0^\circ$)	0.91	0.14
pure-plunge 8° ($h/c = -0.5, 8^\circ$)	1.35	0.15

Due to the inherent shadow between fore- and hindfoils it was not possible to separate the individual forces from each airfoil. Furthermore a time-resolved examination of the blade-vortex interaction using the quasi-steady, combined control-volume analysis was restrictive since the convective information from the forefoil arrived relatively late at the downstream control surface, thus distorting the shape of the force curves in time. In Fig. 8.5 the peak in lift and drag is clearly shifted by $t/T = 0.25$ to the right when compared to the direct-force measurements in Fig. 3.12. Also of interest is the positive offset in lift for those tandem arrangements with $\alpha_H = 8^\circ$. This offset can be explained by the continuous, static lift generated by the hindfoil. Any further insight into the blade-vortex interaction using this control-volume analysis method is limited and therefore the detailed vortical interactions will now be examined by tracking the variation in pressure over the hindfoil surface using the pressure-integration method.

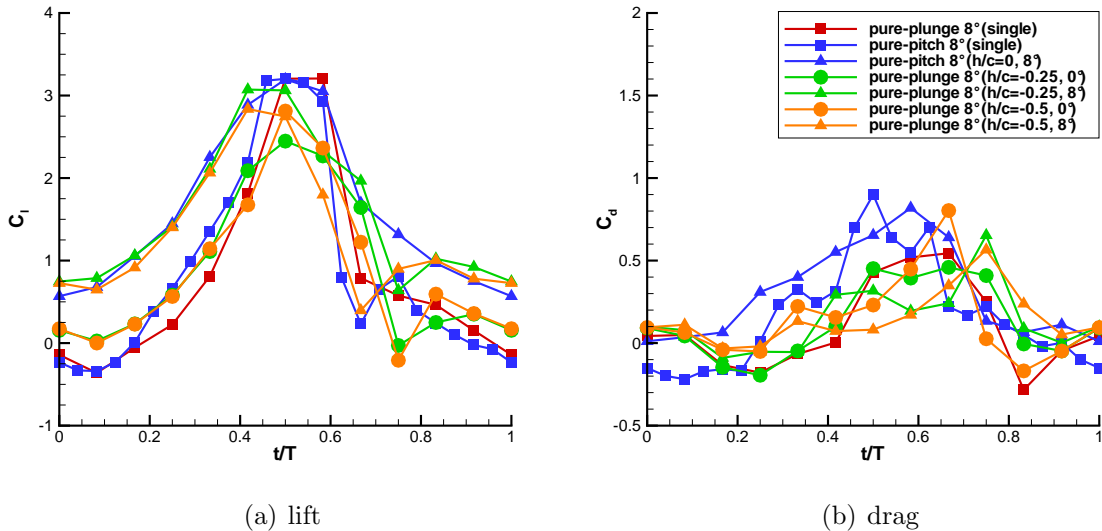


Figure 8.5: Variation of lift (a) and drag (b) using control-volume analysis; note symbols represent measurement phases over the period.

8.2.5 Pressure Integration

In Fig. 8.6 the evolution of the pressure distribution over the hindfoil is plotted for two angles of attack. Note $t/T = 0$ and $t/T = 0.5$ correspond to the top and bottom of the forefoil stroke, respectively. In both instances one can see that a strong suction occurs at $0.333 \leq t/T \leq 0.5$, corresponding to the approaching TEV shown in Figs. 8.3 and 8.4.

The first wave of suction is associated with the passing vortical layer from the trailing edge (counter-clockwise), which in turn generates an upwash on the hindfoil. For the $\alpha_H = 8^\circ$ case, seen in Fig. 8.6(b), a strong vortex-induced separation is generated at the hindfoil's leading edge, corresponding to the proximity of the TEV at the leading edge ($t/T = 0.5$). The overall increase in leading-edge suction over this period accounts for the reduction in net drag. The net lift as reported on in Table 8.1, however, is unchanged when compared to the individual cases and can be explained by the increase in separation once the LEV and TEV have passed downstream. After the convection of the vortex pair, the flow gradually returns to its quasi-steady state by $t/T = 0.75$.

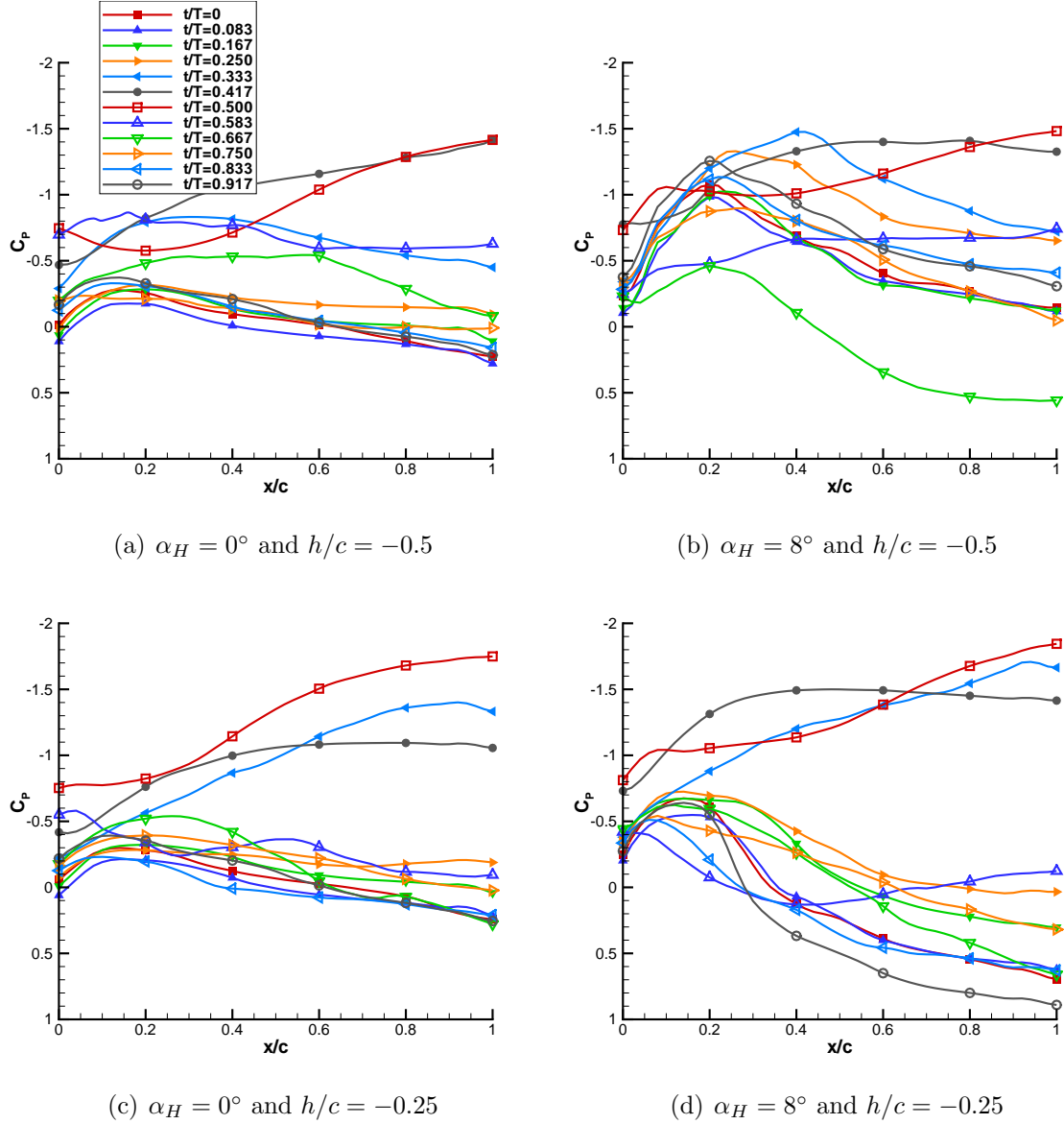


Figure 8.6: Pressure distributions over hindfoil surface for the various tandem configurations demonstrating blade-vortex interaction.

8.3 Summary

The blade-vortex interaction in a Schmidt-propeller configuration has been investigated using PIV. Vortex trajectories, velocities and circulation, combined lift and drag forces as well as pressure distributions over the hindfoil have all been extracted from their re-

spective velocity fields. The control-volume analysis has shown that the combined mean lift for the tandem cases is not increased over the period through blade-vortex interaction. However, a combined mean drag reduction is apparent for certain configurations and can be attributed to leading-edge suction on the hindfoil. The spatial and temporal variation in pressure over the hindfoil associated with the passing vortical wake is extracted using the pressure-integration method and provides further insight into the leading-edge suction mechanism.